CFD–based erosion and corrosion modeling in pipelines using a High–order discontinuous Galerkin multiphase solver

C. Redondo*[a], **M. Chávez–Modena***[a], **J. Manzanero**[a], **G. Rubio**[a], **E. Valero**[a], **S. Gómez–Álvarez**[b], **A. Rivero–Jiménez**[b]

[a]*ETSIAE–UPM - School of Aeronautics, Universidad Politécnica de Madrid. Plaza Cardenal Cisneros 3, E-28040 Madrid, Spain.,*
Center for Computational Simulation, Universidad Politécnica de Madrid, Campus de Montegancedo, Boadilla del Monte, 28660, Madrid, Spain.
** carlos.redondo@upm.es, * m.chavez@upm.es*
[b]*Repsol Technology Lab Agustín de Betancourt S/N, 28935, Móstoles, Madrid, Spain*

Abstract

We present a Computational Fluid Dynamics (CFD)–based methodology for the modeling of erosion and corrosion in hydrocarbon pipes. The novelty of this work is the use of a high–order Discontinuous Galerkin Spectral Element Method (DGSEM) approximation of the incompressible Navier–Stokes/Cahn–Hilliard model for the CFD simulation. This technique permits a very detailed three dimensional representation of the flow regime, phases distribution and contact surfaces that conform the pipe, which results in accurate computations of erosion and corrosion rates and distribution over the pipeline surface.

The developed methodology is validated with experiments relevant for oil and gas industry. In particular, we simulate the erosion in a one–phase ascending pipe with two elbows and the corrosion in a two–phase pipe under several flow regimes.

Keywords: Computational fluid dynamics, Phase–field, High–order Discontinuous Galerkin, Erosion, Corrosion, Pipelines, Multiphase flow.

1. Introduction

The transportation of hydrocarbons is characterized by the presence of multiphase flow, usually containing a mixture of liquid crude oil, natural gas, water and sand particles. This transport may result in the wear of the pipe due to phenomena such as erosion and corrosion. On the one hand, erosion usually occurs as a result of the transport of the fluids with entrained solid particles. The erosion is caused when these particles, dragged by the fluid, hit violently the wall of the pipe, begin able to remove part of its material. On the other hand, multiphase flows usually contain acidic chemical components, such as CO_2 or H_2S, dissolved in the aqueous phase. Corrosion appears if those components get in contact with the walls at certain pressure, temperature and shearing conditions. Both erosion and corrosion can be responsible for failure of the equipment, transport pipelines and production tubing. The prediction of these phenomena permits to estimate the operating life and to identify the locations where severe wear is likely to occur. For example, elbows and plugged tees, which are typically used in piping systems to redirect fluids, are particularly vulnerable to erosion when sand particles are present.

Erosion is a highly complicated phenomenon with a wide range of factors contributing to its severity (e.g. fluid flow and particles rates, properties of the fluid, properties of the particles, wall material or particle impingement angle). A variety of erosion models have been developed to predict this phenomenon. Most methods are based on a limited amount of experimental data, and therefore are only applicable to specific conditions. The use of general guidelines (e.g. American Petroleum Institute Recommended Practice 14E (API RP 14E) [1]) conduces to too conservative designs for most of the situations. Although the accuracy of these general guidelines can be improved (see for example [2, 3, 4, 5]), it is required to have detailed data on the velocity of the particles and their impact angle to really refine the prediction of the erosion rate and its location. Following this idea, McLaury [6] proposed a generalized erosion prediction procedure that involves flow simulation, particle tracking, and erosion modelling, which is now generally known as Computational Fluid Dynamics (CFD)–based erosion prediction [7, 8, 9]. Erosion models are key to get accurate results using CFD–based erosion prediction. Finnie's erosion model [10] has been employed by many authors in

the past to compute the erosion ratio, but it is necessary to adjust correctly the empirical parameters to obtain accurate results [11, 12, 13]. In contrast, there are more advanced models (see for example Oka's model [14]) that can provide precise results avoiding many empirical parameters [15, 16, 17]. The use of CFD–based erosion prediction techniques on industrial systems allow to minimize erosion damages and to optimize the pipe geometry and the flow conditions. For example, see [18, 19] where an optimization of the pipe geometry was conducted to reduce the erosive wear.

Corrosion in steel pipes mainly depends on the presence of an aqueous phase in contact with the pipe. Most of the published models for pipeline internal corrosion apply for sweet corrosion only [20, 21]. However, the water and the oil phases can be either mixed (e.g. emulsions) or separated (e.g., stratified, slug or annular regimes). The fluid flow regime, which depends on the properties of the fluids, water cut, or the pipe geometry and inclination, will determine if the pipe is wetted by either oil or the corroding aqueous phase [22]. Besides, the pipe corrosion can be modeled by a combined effect of electro–chemical reactions, mass transfer and wall shear stress. As a result, sweet corrosion of steels should include the influence of fluid mechanics [23, 24, 25, 26].

In this work, we propose a methodology to predict the erosion and corrosion in pipes using a multiphase CFD technique. We solve the flow field with the method described by Manzanero et al. [27]. This method uses a three–phase phase–field approach coupled with the incompressible Navier–Stokes equations to describe the flow in pipes with (up to) three inmiscible phases. Compared to other interface capturing methods such as Volume of Fluid [28] or Level Set [29], phase field methods (also known as diffuse interface methods) [30, 31, 32] provide a useful alternative that overcomes the most commonly found problems as mass conservation or the accurate computation of the surface tension. In diffuse interface methods, a phase–field function that describes the N–phase system is defined. The sharp fluid interface is replaced by a smooth transition layer that connects the two inmiscible fluids. The evolution of the phase–field function in [27] is modeled by means of the convective Canh–Hilliard equation [33], in particular with the model of Boyer et al. [34].

The three–phase model in [27] is numerically approximated in space with a high–order Discontinuous Galerkin Spectral Element Method (DGSEM) [35] that uses the symmetric interior penalty method [36, 37, 38, 39, 40]. The DGSEM has been used in the past to discretize multiphase (two phase) flows [41, 42, 43, 44, 45], and it is popular because of its arbitrary order of accuracy [46, 35], its low dissipative and dispersive errors [47, 48, 49, 50], the ability to represent arbitrarily three–dimensional complex geometries through the use of unstructured meshes with curvilinear elements [51], efficient mesh adaptation techniques [52, 53, 54], and the design of provably stable schemes [55, 56, 57, 58, 59, 60, 44].

Previous studies of the erosion and corrosion have used CFD techniques to predict the flow behaviour. However, they use low order methods implemented in commercial solvers such as ANSYS–Fluent, or CFX (e.g. [7, 8, 9] for erosion prediction or [61, 26] for corrosion prediction). To the best of the authors' knowledge, this is the first work that uses a phase–field model discretized with a high–order CFD method for the prediction of the erosion and corrosion. The phase–field model has one advantage compared to their counterparts, as it permits to model phase separation, even in the absence of gravity effects. This is important as no special inlet boundary condition must be imposed, the phases may enter in the pipeline mixed, and the separation will occur as the flow develops in the simulation domain. From the advantages of high order methods previously enumerated, we highlight the enhanced representation of the geometries. The latter results is an improved prediction of the particles impact angles and the wall shear stress, with a subsequent more accurate estimation of the erosion and corrosion. It should be noticed that the CFD method chosen [27] permits to solve up to three phases flow simulations. This is interesting for hydrocarbon transport pipes, where water, liquid oil and natural gas can be found. However in this work we restrict ourselves to two–phase simulations.

The content of this text is organized as follows. First, Section 2 introduces the numerical methodology to predict the flow regime, and based on the flow variables obtained, compute corrosion and erosion. Then, Section 3 includes numerical experiments to validate our erosion and corrosion toolchain computation. Finally, Section 4 summarizes the main conclusions of the work.

2. Methodology

2.1. Computation of the fluid flow field. Flow simulation

In this section we describe the equations that govern the evolution of the flow variables, and their numerical approximation. The numerical method used is fully described in previous works: see [62] for the discretization of the three component Cahn–Hilliard equation and [27] for the discretization of the three phase flow model. The methodology is implemented in a flexible solver that handles general unstructured high order meshes. In this work, for simplicity we only summarize those schemes, referring the reader to the previous references for details.

We use the incompressible Navier–Stokes/Cahn–Hilliard model of [27]. Although this model can solve up to three–phase flows, we restrict ourselves to its two–phase variant. The model is a diffuse interface phase field method, which introduces a scalar field that represents the volume fraction, or concentration, of each of the phases in a continuous fashion, $c(\mathbf{x}, t)$. The concentration typically ranges from 1 (Phase 1) to 0 (Phase 2). Across the interface, the thermodynamic variables (e.g. density and viscosity) face a smooth transition from their values in one phase to the other (assumed constant values),

$$\rho\left(c\right) = \rho_1 c + \rho_2\left(1 - c\right). \tag{1}$$

The evolution of the concentration follows the convective Cahn–Hilliard equation

$$c_t + \vec{\nabla} \cdot (c\mathbf{u}) = M_0 \vec{\nabla} \cdot \left(\vec{\nabla}\mu\right), \tag{2}$$

where the chemical potential,

$$\mu = \frac{24\sigma}{\varepsilon}\left(c(1-c)^2 - c^2(1-c)\right) - \frac{3}{2}\sigma\varepsilon\vec{\nabla}^2 c, \tag{3}$$

is driven by a double–well chemical free–energy. In (3), σ represents the interface tension coefficient between the phases. The size of the interface is effectively controlled by the *interface width*, ε, a parameter of the model whose value is limited in practice by the mesh resolution. The Cahn–Hilliard equation includes antidiffusive and diffusive chemical effects. On the one

hand, the antidiffusion is introduced by the chemical free–energy, which favors phase separation and it is one of the features that makes this model attractive. This enables the possibility to initialize the solutions from a homogeneous mixture of the phases, and then let the phases to grow, evolve, and coalesce naturally. On the other hand, the diffusion is known as the interfacial energy, and it is responsible for the regularization of the antidiffusive effects. The strength of one term over the other depends on the interface width ε parameter,

$$\varepsilon \propto \frac{\text{diffusive}}{\text{antidiffusive}}, \tag{4}$$

such that increases of ε stabilize the solution at the expense of a wider interface.

A final remark on the Cahn–Hilliard equation, is that the concentration is driven by two effects: convection and the chemical diffusion. If the convection dominates over the chemical diffusion, the flow is not able to fully perform phase separation and the phases tend to remain dispersed. On the contrary, if the chemical diffusion dominates, the strength of the interface is too high and the velocity field cannot warp the bubbles formed. Therefore, we seek for a delicate balance between these two effects, controlled with a constant parameter called *mobility*, M_0,

$$M_0 \propto \frac{\text{chemical diffusion}}{\text{convection}}. \tag{5}$$

For more details on the proper selection of the mobility parameter, see [63].

Unlike conventional methods which rely in the Reynolds–Averaged Navier–Stokes (RANS) equations to compute the velocity field, an implicit Large Eddy Simulation (LES) approach [64] is adopted in this work, where the numerical viscosity of the scheme acts as a subgrid filter. The LES methodology results in a more accurate treatment of turbulent effects, with the disadvantage of requiring more spatial resolution. For a comparison of RANS and LES approaches in one phase pipe simulations see [65]. The velocity field $\mathbf{u}(\mathbf{x}, t)$ is obtained from the momentum equation, which incorporates a volume approximation of the capillary forces

$$(\rho\mathbf{u})_t + \vec{\nabla}\cdot(\rho\mathbf{u}\mathbf{u}) = -\vec{\nabla}p + \mu\vec{\nabla}c + \vec{\nabla}\cdot\left(\eta\left(\vec{\nabla}\mathbf{u} + \vec{\nabla}\mathbf{u}^T\right)\right) + \rho\mathbf{g}. \tag{6}$$

In (6), η is the viscosity, computed from the (constant) equilibrium phases viscosities $\eta_{1,2}$ in a similar fashion to the density (see (1)). The term $\mu\vec{\nabla}c$ is the phase field approximation of the capillary pressure [66], and $\mathbf{g}$ is the gravity acceleration.

Finally, the pressure is computed from an artificial compressibility model [67, 68, 69] as:

$$p_t + \rho_0 c_0^2 \vec{\nabla} \cdot \mathbf{u} = 0, \tag{7}$$

with $\rho_0 = \max(\rho_1, \rho_2)$ and c_0 the artificial compressibility sound speed.

The equations are approximated with a high–order Discontinuous Galerkin Spectral Element Method (DGSEM) [35]. This method is convenient since it provides arbitrarily high order accurate schemes while maintaining geometrical flexibility through the use of unstructured meshes. The conservation laws are written in a conservative fashion similar to finite volume schemes. However, inside every element the solution is approximated by a polynomial function of degree N, which allows the solution to spatially vary within the element in the DG method. One of the main advantages of high–order methods is the spectral convergence, which results in exponential convergence for smooth solutions. This results in less degrees of freedom for the same accuracy, when compared to traditional low order methods [46, 35]. Additionally the operation count of the DGSEM differential operators scales linearly with the polynomial order [70], resulting in a linear growth of run times with the polynomial order for explicit computations, such as the ones conducted in this work. The increase of the polynomial order presents one disadvantage though, which is a steeper limitation of the explicit time step compared to a conventional mesh refinement (the time step for explicit computations scales with h/N^2, where h is the size of the element and N the polynomial degree used in the computation see [46]). Of course, this limitation could be bypassed by using implicit time integrators with a dual time step strategy, which is not considered in this work. Besides, high–order schemes present additional advantages such as their low numerical dissipation, a higher–order approximation of the geometry (e.g. retaining the curvature see Appendix A), their compact stencils, and all without comprising their robustness [71, 72, 59, 44],

as they can be constructed provably stable. The thorough details of the incompressible Navier–Stokes/Cahn–Hilliard system approximation can be found in [27].

2.2. Erosion computation

To predict the erosion, we firstly inject a number of particles in the flow, whose trajectories are then calculated. Secondly, the erosion produced by each individual particle impact onto the pipe wall is computed. Finally, the erosion rate and particle impact statistical parameters are interpolated onto a fine surface mesh. The tracking of the particles is performed over an averaged flux using a one–way coupling, i.e. it assumes no interaction between particles and no influence of the particles in the fluid flow. For more advanced approaches, where inter-particle collisions are considered see [73, 74]. However, this one–way coupling has proven accurate enough for particle laden flows where the mass fraction of the disperse phase is low.

2.2.1. Particle tracking

Particles are assumed spherical and with no interactions among them. Under these assumptions, the dynamics of the particles is described by the momentum equation:

$$\frac{d\mathbf{u}_p}{dt} = \mathbf{g}\frac{\rho_p - \rho}{\rho_p} - \frac{1}{2}\frac{\rho C_d A_{p,c}}{m_p}(\mathbf{u}_p - \mathbf{u})|\mathbf{u}_p - \mathbf{u}|, \tag{8}$$

where ρ_p is the particle density, $\mathbf{u}_p$ is the particle velocity, $\mathbf{g}$ is the gravity, C_d is the drag coefficient (a function of the Reynolds number, Re), $A_{p,c}$ the particle cross–sectional area and m_p is the particle mass. Fluid velocity, $\mathbf{u}$, and density, ρ, are interpolated to the position of the particle from the fluid field. Additionally, the momentum equation takes into account buoyancy effects.

As the velocity of the particles is known, the particle position, $\mathbf{x}_p$, can be determined from the equation, $\frac{d\mathbf{x}_p}{dt} = \mathbf{u}_p$. The drag coefficient is computed using the Brown and Lawler formula for spherical particles [75],

$$C_d = \frac{24}{Re_D}(1 + 0.15Re_D^{0.681}) + \frac{0.407}{1 + \frac{8710}{Re_D}}, \tag{9}$$

valid for the subcritical region $Re_D < 10^5$, with

$$Re_D = \frac{\rho|\mathbf{u}_p - \mathbf{u}|2r_p}{\eta}, \tag{10}$$

where η is the dynamic viscosity of the mixture interpolated from the fluid field and r_p the particle radius.

Finally, for the bounce of the particles, the Sommerfeld virtual wall model with random orientation [76] is used to model the pipe wall roughness. We use a deterministic approach for the normal coefficient of restitution (e_n) and tangential coefficient of restitution (e_t). The impact velocity is split into the normal $\mathbf{u}_{1,n}$ and tangential $\mathbf{u}_{1,t}$ components with respect to the virtual wall. Then the components of the particle velocity after the collision $\mathbf{u}_{2,\mathbf{n}}$ and $\mathbf{u}_{2,\mathbf{n}}$ are calculated with the expression

$$\begin{aligned} \mathbf{u}_{2,n} &= -e_n \mathbf{u}_{1,n} \\ \mathbf{u}_{2,t} &= e_t \mathbf{u}_{1,t}. \end{aligned} \tag{11}$$

For the coefficients of restitution a simple two parameters model is used. The coefficient, e, is 1 for zero impact angle and decreases linearly with the impact angle θ up to a limit angle θ_e. After that, it remains constant with value e_h for impact angles higher than θ_e,

$$e = \begin{cases} 1 - \frac{(1-e_h)}{\theta_e}\theta & \theta \leq \theta_e \\ e_h & \theta > \theta_e. \end{cases} \tag{12}$$

The parameters for the normal ($\theta_{e,n}, e_{h,n}$), and tangential ($\theta_{e,t}, e_{h,t}$) components are adjusted to fit experimental data. The numerical values of the parameters used in this work are specified in Sec. 3.1.1.

2.2.2. Computation of erosion and penetration rates

The erosion of a pipeline is estimated by calculating the erosion caused by a sufficient number of individual particles to be statistically representative. According to the Finnie's model of 9 parameters [11, 12, 13], the *erosion ratio*, ER (kilograms of eroded material per kilogram of impacting material, ($\mathrm{kg\,kg^{-1}}$)) is defined as

$$ER = k|\mathbf{u}_1|^n f(\theta), \tag{13}$$

where $\mathbf{u}_1$ is the particle impact velocity, $f(\theta)$ is a function of the impact angle, θ,

$$f(\theta) = \begin{cases} a\theta^2 + b\theta, & \theta \leq \theta_0 \\ x\cos^2\theta\sin(\omega\theta) + y\sin^2\theta + z, & \theta > \theta_0 \end{cases}, \tag{14}$$

and $k, n, a, b, x, w, y, z, \theta_0$ are empirical parameters that depend on the eroded material. In this work, the aluminium material values are used for the model constants (more details are given in Section 3.1.1).

We define two parameters of interest in erosion computations: the *penetration rate* ($\mu\text{m}\,\text{kg}^{-1}$ or $\text{mil}\,\text{lb}^{-1}$) and the erosion per unit of time and surface or *erosion rate* ($\text{kg}\,\text{m}^{-2}\,\text{s}^{-1}$). These parameters are defined for a certain computational cell i by the expressions:

$$\begin{aligned} \text{penetration rate}_i &= \frac{\sum_1^{n_p} ER_j m_j}{M_t a_i \rho}, \\ \text{erosion rate}_i &= \frac{\dot{m}\sum_1^{n_p} ER_j m_j}{M_t a_i}, \end{aligned} \tag{15}$$

where ER_j and m_j are the erosion ratio and the particle mass for the impact j, n_p is the number of impacts in cell i, M_t is the total mass of particles injected in the simulation, $\dot{m}$ is the particles mass flow to be simulated, a_i is the cell area and ρ the density of the pipe material.

2.3. Computation of corrosion

The *corrosion rate*, *CR* ($\text{mm}\,\text{year}^{-1}$), is defined following the Kanwar model [77] as:

$$CR = kP_{\text{CO}_2}^c \tau^b, \tag{16}$$

where τ is the shear stress on the wall computed from the flow variables, $P_{\text{CO}_2}(\text{MPa})$ is the partial pressure of CO_2 and k, b and c are the non–dimensional parameters of the model. The parameters shown in Table 1 are valid for a carbon steel pipe. These values have been used in this work.

Corrosion is only active if there is free water phase in contact with the wall. Our CFD–based corrosion modeling approach predicts the amount of water (c_w) in contact with the wall at each time step. The parameter c_w ($c_w = c$ in (2)) varies continuously from 0 (oil) to 1 (water), and represents the volume of water in a cell divided by the volume of the cell. We propose to

Table 1: Parameters of the Kanwar model [78]

P_{CO_2}, [MPa]	0.27
k	15.5
b	0.1
c	0.83

establish a threshold for the activation of the corrosion process. In particular, we define the following step function,

$$CR_{step} = \begin{cases} 0 & c_w \leq 0.25 \\ CR_k & c_w > 0.25 \end{cases}, \tag{17}$$

where CR_k is the corrosion obtained through expression (16). The value of 0.25 for the concentration, or volumetric fraction, of water, c_w, was selected because it showed good performance in preliminary tests, and remains unchanged for all the test cases.

3. Numerical experiments

In this section we focus on the validation of the methodology using relevant test cases for the oil and gas industry. In particular, we simulate the erosion in a one–phase ascending pipe with two elbows and the corrosion in a two–phase pipe under different flowing conditions.

3.1. Erosion

The methodology to predict the erosion described in Section 2 is validated with the test case presented by Chen et al. [11]. This validation consists of three main parts: flow simulation (Section 2.1), particle tracking and erosion calculation (Section 2.2).

3.1.1. Setup

The validation case consists of a 1 inch diameter pipe ($2.54 \cdot 10^{-2}$ m) with an initial horizontal section of 2.13 m, an ascending vertical section of 1.22 m, and a horizontal outlet section of 0.91 m. The sections are joined by elbows of 90 deg and curvature ratio ($r/D = 1.5$). The material used in the pipe is

pure aluminum. A scheme of the case geometry is shown in Figure 1. A flow of air carrying sand particles is established between the inlet and the outlet of the pipe. The simulation parameters used are shown in Table 2. They replicate the experiment detailed in [11] with inflow velocity of 150 ft/s and particle flow rate of 40 lb per day.

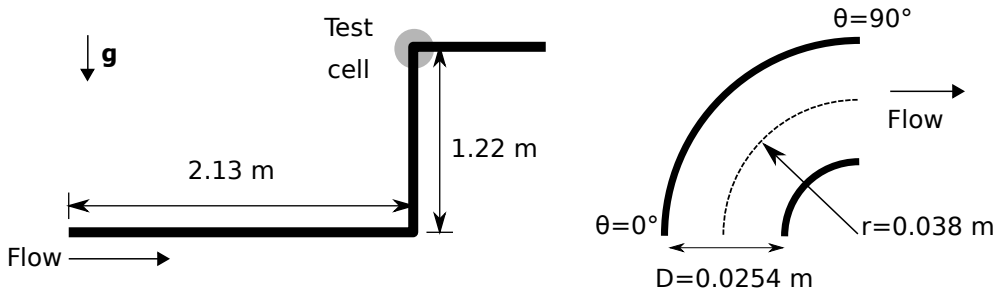

Figure 1: Scheme of the pipe geometry and location of the test cell [11]

Table 2: CFD simulation parameters

Fluid	Air
Velocity inlet, $[\mathrm{m\,s^{-1}}]$	45.72
Density, $[\mathrm{kg\,m^{-3}}]$	1.225
Kinematic viscosity, [Pa s]	$1.85 \cdot 10^{-5}$
Particles diameter, [m]	$1.5 \cdot 10^{-4}$
Particles density, $[\mathrm{kg\,m^{-3}}]$	2650
Particle mass fraction, [-]	$7.44 \cdot 10^{-3}$
Pipe material	Pure aluminium
Density pipe material, $[\mathrm{kg\,m^{-3}}]$	2700
Gravity, $[\mathrm{m\,s^{-2}}]$	9.8

For the fluid flow field computation, a CFD simulation has been carried out on a mesh of 3680 elements with polynomial order 4 (460000 degrees of freedom). A convergence analysis, not included here, shows a good compromise between accuracy and computational cost for this mesh. The particle volumetric fraction in the experiment is $3.4 \cdot 10^{-6}$, such that the interaction between particles and fluid flow turbulence is low [79] and the effect of the

particles on the mean flow is negligible. In this scenario, the use of the one–way fluid–particle coupling model is justified. The particle tracking for the erosion calculation has been performed with 100000 particles. According to numerical experiments in [11] the variation in erosion prediction is negligible for a number of particles above 50000. The particle tracking calculation is computed on a steady solution. A time step of $5 \cdot 10^{-3}$ s is used for the particle tracking integration. This time step permits an accurate computation of the rebounds of the particles.

The parameters of the coefficient of restitution Eq. (12), shown in Figure 2, have been estimated using Reagle's [80] and Sommerfeld's experimental data [76]. More advanced parameters such as the coefficient of friction [74] were not considered for this model.

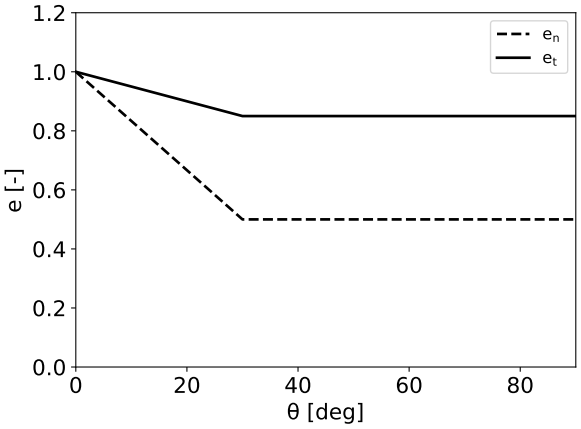

Figure 2: Normal and tangential coefficient of restitution in function of the impact angle used in the simulations [76]

Finally, the parameters of the erosion model used in the simulation are shown in Table 3. References [12, 13] have been used to define two different set of erosion model parameters ([12] for Simulation #1 and [13] for Simulation #2) for the same configuration under study. Following the original works [12, 13], velocity, $\mathbf{u}_1$, in (13) enters in $\mathrm{ft\,s^{-1}}$ in Simulation #1 and in $\mathrm{m\,s^{-1}}$ in Simulation #2.

Table 3: Erosion model parameters

	Simulation #1 [12]	Simulation #2 [13]
k	$2.056 \cdot 10^{-8}$	$1.7 \cdot 10^{-8}$
n	1.73	2.3
a	-34.79	-7.0
b	12.3	5.45
x	0.147	0.4
y	-0.745	-0.9
z	1.0	1.556
ω	5.205	-3.4
θ_0, [deg]	10	23

3.1.2. Results

The results obtained with the CFD–based erosion computation is split into the three segregated steps used for the calculation: flow simulation, particle tracking and erosion calculation.

Flow simulation

The CFD solution has been analyzed after 200000 iterations and approximately 3 times the residence time for the fluid in the pipe, enough to develop a representative flow structure as shown in Figure 3. The simulation took 41h of computational time in 20 Intel Xeon Gold 6230 cores at 2.1 GHz in the CESVIMA-UPM supercomputer center. The mesh used is valid for a Large Eddy Simulation (LES) description of the flow, which is adequate for this application. A time-average of the flow variables is computed using 10 snapshots over a period of 100000 iterations, which corresponds with 0.1 s of physical time using a time step of $1 \cdot 10^{-6}$ s. Particles are integrated over this averaged flow.

Particle tracking

Particles are injected in the initial section and integrated along the pipe. The injected particles collide with the first bend and bounce multiple times in the upstream section of the pipe. As a result, they reach the second bend

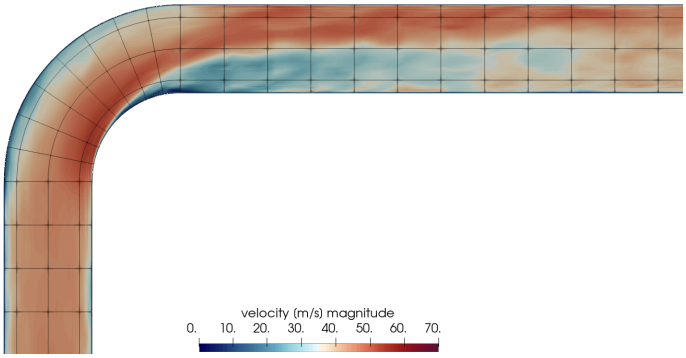

Figure 3: Velocity magnitude contours in the middle section of the pipe in the second elbow corresponding to the test section

practically in line with the main flow but with an appreciable loss of velocity, due both to gravity and to the loss of energy in the successive bounces. In Figure 4 the detail of the particle trajectories in the upper elbow is shown. More than 2 million impacts have been analysed in each simulation.

Erosion calculation

In Figure 5 we detail the erosion results, which feature the characteristic V–shape scar on the elbow. Let us mention that the shape of the erosion scar is associated with the treatment of the wall, the V-shaped scar at the elbow appears with a smooth wall, once the wall becomes rough this characteristic shape changes [81]. Besides, such erosion pattern can be deteriorated if inter-particle collisions are considered with the Discrete Phase Model for higher mass loadings [74, 82]. Comparison with experimental results of Simulations #1 and #2 are shown in Figure 6. The erosion rate in the external mean section of the second elbow is represented together with the experimental results with a good agreement. A similar simulation is presented, along with the experimental results, in [11]. The simulation results shown in Figure 6 are better than those obtained in that work, where the predicted erosion was 10 times higher than the measured. We believe that the lack of agreement between simulation and experiments in [11] might be due to an inappropriate

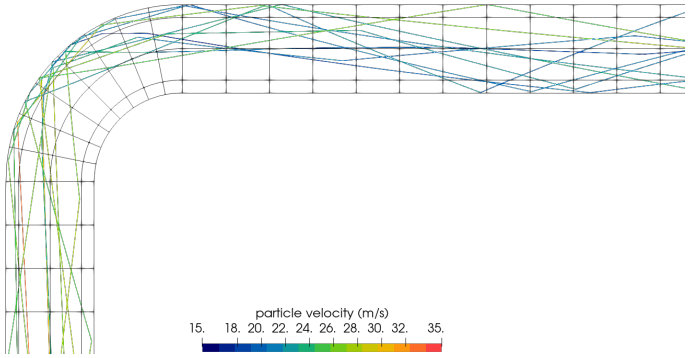

Figure 4: Detail of the particle trajectories in the upper elbow. The color of the trace represents the speed of the particle

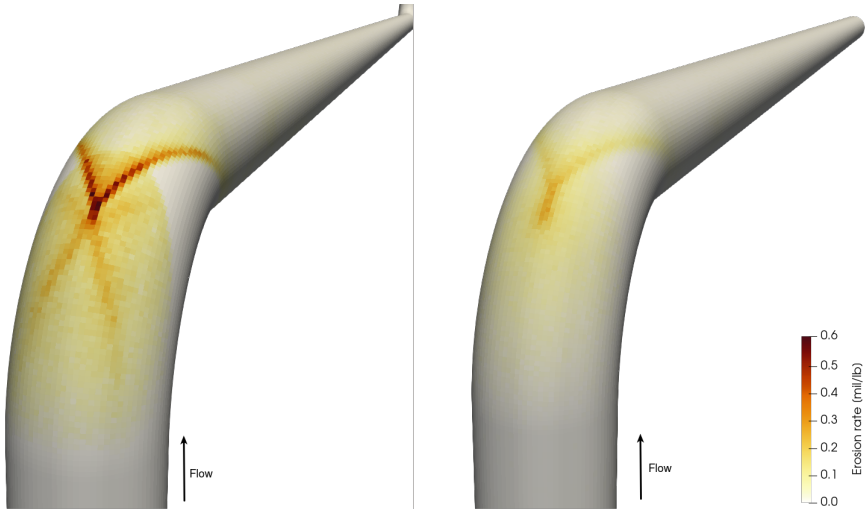

Figure 5: Estimated erosion rate in the first (left) and second (right) elbow for the Simulation #1

selection of a parameter in the model. In particular, the constant k in Finnie's model is not specified in [11], so that might be the source of the discrepancy.

In summary, we confirm the capabilities of the developed method to estimate erosion. This methodology comprises the flow simulation, the particle tracking and the erosion computation through a model that takes into ac-

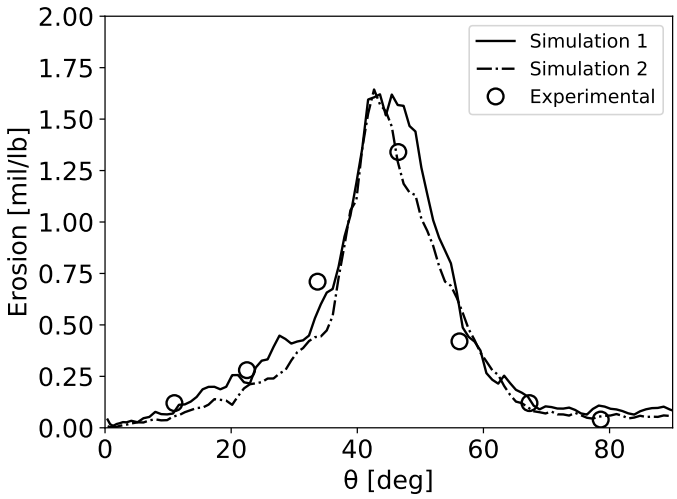

Figure 6: Penetration rate prediction ($\mathrm{mil\,lb^{-1}}$) in the second elbow for Simulations #1 and #2 compared with experimental results from [11]

count the impact of a high number of particles. The erosion rate results have shown the importance of the model parameters (especially the parameter k). Finally a qualitative examination of the effect of the accurate representation of the surface of the pipe, allowed by the high order method used, is included in Appendix A.

3.2. Corrosion

In this section, the methodology introduced in Section 2.3 for the corrosion prediction is validated in carbon steel pipelines at different flow regimes using the experimental data presented by Kanwar [77].

3.2.1. Setup

For the validation of the corrosion model, a simulation of a carbon steel straight pipe of 5 m long and 0.1 m diameter filled by a mixture of oil (Arcopac90) and water is chosen. As previously mentioned, the flow regime depends on the amount of water and oil entering the pipe, so we define $V_{o/w}[\%]$ as the volume flow rate of oil over the total volume flow rate and $V_{w/o}[\%]$ as the volume flow rate of water over the total volume flow rate. Figure 7 [26] illustrates the flow patterns of the oil–water two phase fluid in pipelines with a mean flow velocity, U_0, where $V_{os} = V_{o/w}U_0$ and $V_{ws} = V_{w/o}U_0$ are oil superficial velocity and water superficial velocity, respectively.

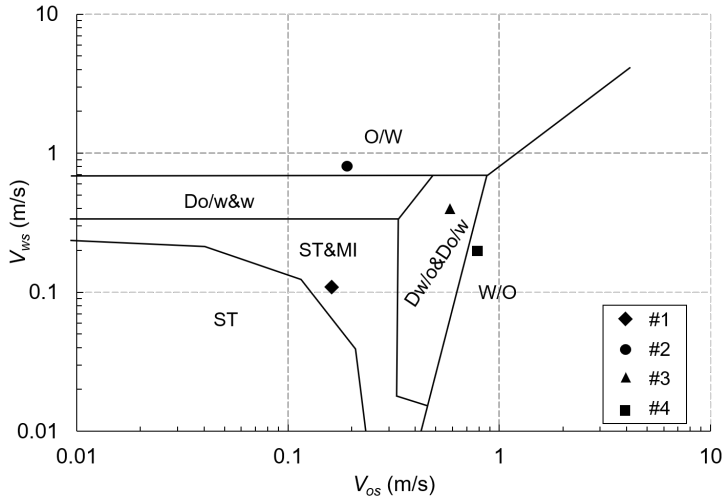

Figure 7: Flow pattern of the oil–water two phase fluid in pipelines [26] and numerical simulations. ST is stratified flow, ST & MI is stratified flow with mixing on the pipe wall surface, O/W is oil in water emulsion, W/O is water in oil emulsion, $D_{o/w\&w}$ is dispersion of oil in water emulsion and water, and $D_{w/o}$ & $D_{o/w}$ is dispersion of water in oil and oil in water

For this validation four different regimes have been selected (labeled from

#1 to #4 in Figure 7). For each one, a CFD simulation will be performed to get the flow regime and the flow variables in the domain; after that, the corrosion rate will be computed following Section 2.3 and compared with experimental results.

The fluid properties used for the simulation are shown in the Table 5. After a detailed convergence analysis, not included here, the simulation has been carried out on a mesh of 2800 elements (140 sections of 20 elements) and polynomial order 4 (see Figure 8). The resolution of this mesh permits to capture the interfaces between the two phases with an interface width, $\varepsilon = 0.01\,\mathrm{m}$. Finally, the mobility is set to $M_0 = 8 \cdot 10^{-7}\,\mathrm{m^3 kg^{-1} s}$, which results in an appropriate balance between convection and chemical diffusion effects. Additionally, a low value of this parameter is beneficial from a numerical point of view, as it reduces the stiffness of the resulting system of equations. For more details on the proper selection of the mobility parameter, see [63].

Table 4: Parameters for the four different CFD–based corrosion prediction simulations

Simulation	#1	#2	#3	#4
Flow regime	ST & MI	O/W	$\mathrm{D_{w/o}}$ & $\mathrm{D_{o/w}}$	W/O
$V_{o/w}$, [%]	60	20	60	80
U_0, $[\mathrm{m\,s^{-1}}]$	0.28	1	1	1

Table 5: Fluid properties for the CFD–based corrosion computations

	Water	Arcopac90
Density, $[\mathrm{kg\,m^{-3}}]$	992.25	825.0
Kinematic viscosity, $[\mathrm{Pa\,s^{-1}}]$	$0.653 \cdot 10^{-3}$	$15.0 \cdot 10^{-3}$
Surface tension, $[\mathrm{N\,m^{-1}}]$	0.028	
Contact angle, [deg]	45	

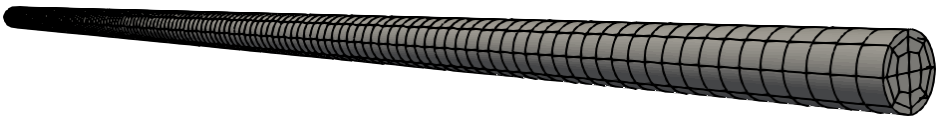

Figure 8: Detail of the high order mesh used for the CFD–based corrosion computations of a straight pipe

3.2.2. Results

This section includes the results for the four simulations detailed in Table 4. The results include the prediction of the flow regime and the computation of the corrosion rate.

Flow simulation

To accelerate convergence and get a representative flow structure, the simulation has been started with 100000 iterations and a polynomial order of 3, followed by 100000 iterations with polynomial order 4. The last 100000 iterations, which correspond with 4 s of physical time using a time step of $2 \cdot 10^{-5}$ s , have been used to perform the post–processing. The simulation took 48h of computational time in 20 Intel Xeon Gold 6230 cores at 2.1 GHz in the CESVIMA-UPM supercomputer center.

According to experimental results [77], for oil volumetric fractions of 60% and below, stratified flow is maintained with a continuous film of water at the bottom of the pipe, causing corrosion in that area. For oil volumetric fractions of 80% and above, the water film breaks down and the water forms a dispersed phase in a continuous oil matrix. With this flow pattern corrosion is dramatically reduced.

Figures 9, 10, 11 and 12 show the flow structures at the different flow regimes. Top view represents the *pure* water representation ($c_w > 0.25$) and the bottom view represents the mixture interface between water ($c_w < 0.25$) and oil ($c_o < 0.25$). The parameters c_w and c_o are obtained from the Cahn–Hilliard equation (2) as $c_w = c$ and $c_o = 1 - c$. All simulations consider a stratified flow in the inflow boundary condition. It is noticeable that the flow needs a distance of 3m to develop completely. This distance will not be taken into account for the corrosion analysis. Figure 9 shows a stratified

flow with mixing at the interface (ST & MI). Figure 10 depicts how the oil is emulsified into the water (O/W). In contrast, the water is emulsified into the oil (W/O) in Figure 12. In this case, it is remarkable how the surface of pipe steel wetted by water is very small, leading to negligible corrosion. Finally, Figure 11 shows a typical dispersed flow of water in oil and oil in water ($D_{w/o}$ & $D_{o/w}$). The flow regimes were correctly predicted (according to experimental data) by our high–order phase–field CFD technique without additional information.

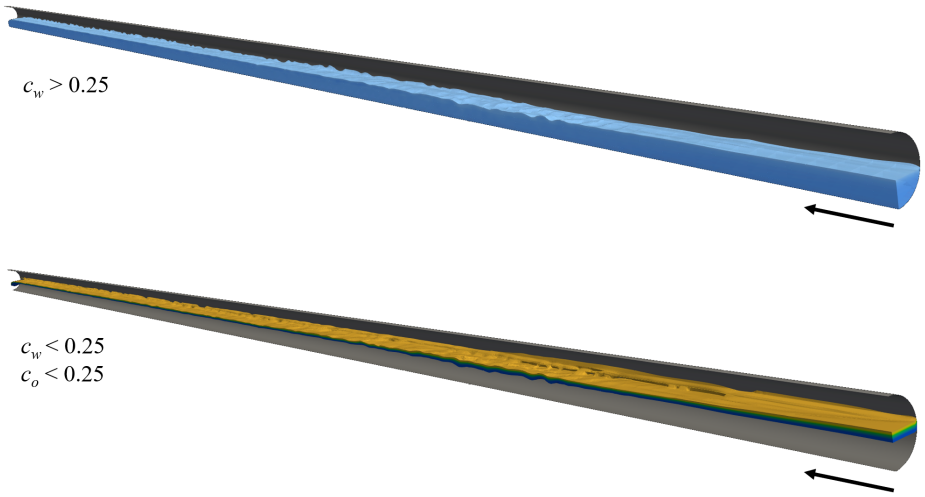

Figure 9: Simulation #1 with stratified flow with mixing on the pipe wall surface (ST&MI) flow regime for $o/w = 60\,\%$ and $U_0 = 0.28\,\mathrm{m\,s^{-1}}$

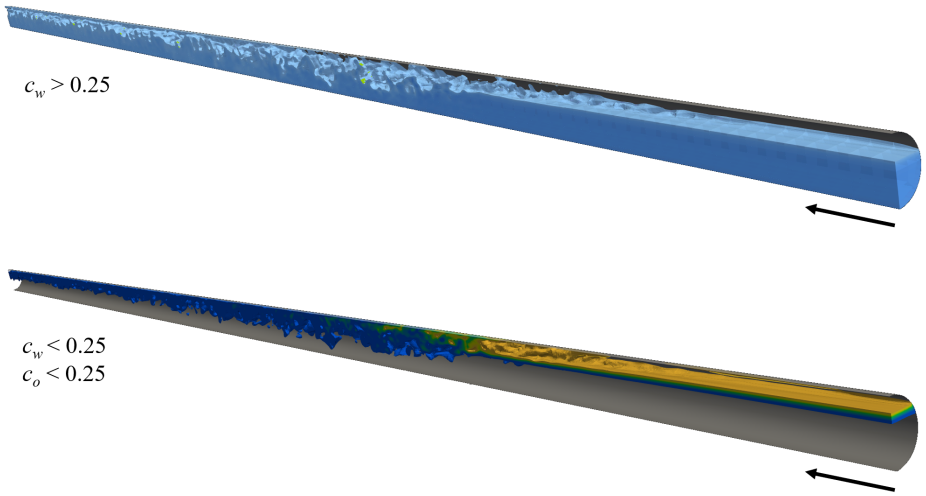

Figure 10: Simulation #2 with oil in water emulsion (O/W) flow regime for $V_{o/w} = 20\,\%$ and $U_0 = 1\,\mathrm{m\,s^{-1}}$

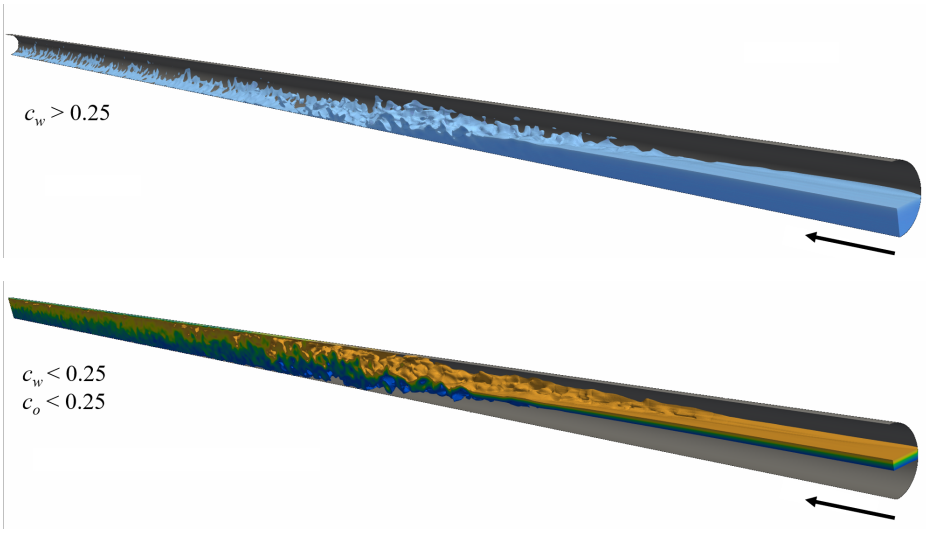

Figure 11: Simulation #3 with dispersion of water in oil and oil in water ($\mathrm{D_{w/o}}$ & $\mathrm{D_{o/w}}$) flow regime for $V_{o/w} = 60\,\%$ and $U_0 = 1\,\mathrm{m\,s^{-1}}$

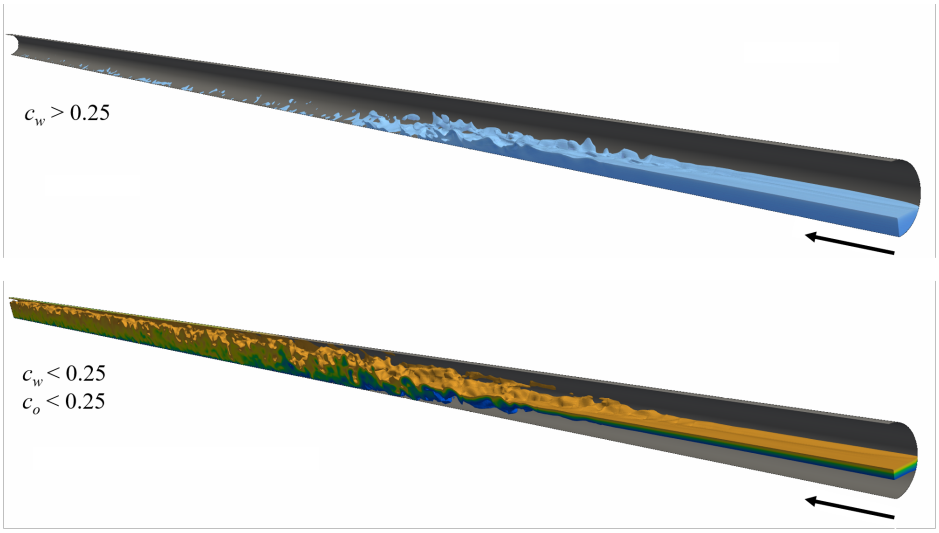

Figure 12: Simulation #4 with water in oil emulsion (W/O) flow regime for $V_{o/w} = 80\,\%$ and $U_0 = 1\,\mathrm{m\,s^{-1}}$

Corrosion calculation

As mentioned before, the estimation of the corrosion rate has been performed using (16) and (17) over 20 time instants corresponding to 4 s of physical time and the average value has been obtained. The corrosion has been analyzed in the section where the flow is developed $3\,\mathrm{m} < x < 4.95\,\mathrm{m}$. The outlet section has been excluded to avoid pollution from the boundary condition in the corrosion rate.

Table 6: Maximum corrosion rate (CR_{max}) and shear in water wetted walls τ_{max}. Numerical results are obtained with our methodology. Experimental results are taken from [77]

			CR_{max} [mm year^{-1}]		τ_{max} [N m^{-1}]	
Sim.	U_0[m s^{-1}]	$V_{o/w}$[%]	Num.	Exp.	Num.	Exp.
#1	0.28	60	4.90	4.70	0.52	0.34
#2	1.00	20	5.57	6.35	6.50	6.98
#3	1.00	60	6.27	6.40	7.80	7.55
#4	1.00	80	-	negligible	-	negligible

The results obtained for the maximum corrosion rate along with the

maximum shear in wet walls is represented in Table 6. The results are in good agreement with the experimental results, showing the validity of the methodology. It is especially noticeable the accuracy in Simulation #4 ($V_{o/w} = 80\,\%$). In this case the water film breaks and the water goes on to form a dispersed phase in the oil and the corrosion is negligible. It has been confirmed that the correct simulation of the flow regime carried with our phase–field high–order CFD technique is paramount for the accuracy of the corrosion rate computation.

4. Conclusions

This work has shown that the methodology presented is able to predict erosion–corrosion in pipes carrying multiphase mixtures. Two test cases relevant to oil and gas industry have been studied, showing the reliability of the incompressible Navier–Stokes/Cahn–Hilliard equations approximated with a high–order Discontinuous Galerkin Spectral Element Method (DGSEM) to solve hydrocarbon transport pipes problems.

As far as erosion modeling is concerned, the results for a one phase complex configuration are very satisfactory. The particles reach the study zone after multiple bounces and an upward path. With the first bounces the particles lose speed and their trajectories become oblique to the main flow. In the upward section the particles align again with the flow and gain speed. Finally they collide with the second elbow eroding the wall section under study. The results show a good behavior of the particle drag model, the rebound model and the erosion model.

As far as corrosion modeling is concerned, the results are also in good agreement with the experiments. In this case, the complexity is not driven by the geometry (a straight pipe is considered) but by the flow pattern. A multiphase experiment is considered where different volumetric fractions of water and oil are used in the inlet boundary. Depending on these volumetric fractions, different flow regimes can be experimentally observed. These regimes are appropriately captured by our CFD methodology, resulting in an accurate computation of the corrosion rate.

Acknowledgement

The authors acknowledge the computer resources and technical assistance provided by the Centro de Supercomputación y Visualización de Madrid (CeSViMa). The authors acknowledge Repsol Technology Lab and Universidad Politécnica de Madrid for their support and permission to publish this work. Gonzalo Rubio and Eusebio Valero acknowledge the funding received by the project SIMOPAIR (Project No. REF: RTI2018-097075-B-I00) from the Ministry of Innovation of Spain. Authors also thank Gabriel Rucabado from Repsol Technology Lab for his assistance during the execution of this work.

Appendix A. High order representation of the surface

Figure A.13 illustrates the effect of the CFD method used to compute the erosion. The usage of a discontinuous Galerkin method, permits a high order representation of the surface. Figure A.13 compares the distribution of the particles impacts using first order surface representation (right) and fourth order surface representation (left). An accurate prediction of the impact angle is critical to estimate the erosion pattern caused by secondary rebounds along the elbow and the single particle erosion that has a highly nonlinear dependency with the incoming angle. As can be seen, the high order method permits to obtain an accurate solution with a low number of elements. This fact is especially relevant in multiphase simulations of complex geometries where a nearly constant mesh refinement is required to capture the interface between the phases.

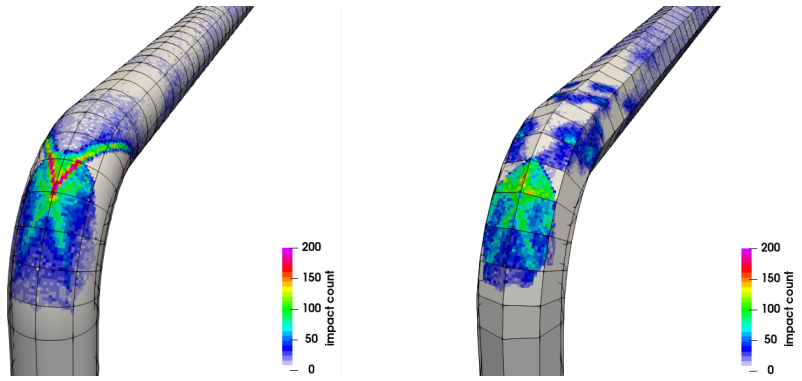

Figure A.13: Influence of the surface polynomial order representation (1st order right, 4th order left) on the impact distribution along the first elbow

References

[1] American Petroleum Institute, API recommended practice for design and installation of offshore production platform piping systems, API RP 14E, American Petroleum Institution, Fifth Edition. Washington DC (October 1991).

[2] S. Nešic, J. Postlethwaite, A predictive model for localized erosion—corrosion, Corrosion 47 (1991) 582–589.

[3] S. Shirazi, J. Shadley, B. McLaury, E. Rybicki, A procedure to predict solid particle erosion in elbows and tees (1995).

[4] S. Shirazi, B. McLaury, J. Shadley, E. Rybicki, et al., Generalization of the api rp 14e guideline for erosive services, Journal of Petroleum Technology 47 (1995) 693–698.

[5] M. M. Salama, An alternative to api 14e erosional velocity limits for sand-laden fluids, J. Energy Resour. Technol. 122 (2000) 71–77.

[6] B. S. McLaury, Predicting solid particle erosion resulting from turbulent fluctuations in oilfield geometries., Ph.D. thesis, 1997.

[7] X. Chen, B. S. McLaury, S. A. Shirazi, Application and experimental validation of a computational fluid dynamics (CFD)-based erosion

prediction model in elbows and plugged tees, Computers & Fluids 33 (2004) 1251–1272.

[8] L. Xu, Q. Zhang, J. Zheng, Y. Zhao, Numerical prediction of erosion in elbow based on CFD-DEM simulation, Powder Technology 302 (2016) 236–246.

[9] S. Karimi, S. A. Shirazi, B. S. McLaury, Predicting fine particle erosion utilizing computational fluid dynamics, Wear 376 (2017) 1130–1137.

[10] I. Finnie, Erosion of surfaces by solid particles, wear 3 (1960) 87–103.

[11] X. Chen, B. S. McLaury, S. A. Shirazi, Application and experimental validation of a computational fluid dynamics (CFD)-based erosion prediction model in elbows and plugged tees, Computers and Fluids 33 (2004) 1251–1272. doi:10.1016/j.compfluid.2004.02.003.

[12] X. Chen, B. S. McLaury, S. A. Shirazi, Numerical and experimental investigation of the relative erosion severity between plugged tees and elbows in dilute gas/solid two-phase flow, Wear 261 (2006) 715–729. doi:10.1016/j.wear.2006.01.022.

[13] H. Hadžiahmetović, D. Kahrimanović, E. Džaferović, N. Hodžić, Computational fluid dynamics (CFD) based erosion prediction model in elbows, Tehnicki Vjesnik 21 (2014) 275–282.

[14] Y. I. Oka, K. Okamura, T. Yoshida, Practical estimation of erosion damage caused by solid particle impact: Part 1: Effects of impact parameters on a predictive equation, Wear 259 (2005) 95–101.

[15] G. C. Pereira, F. J. de Souza, D. A. de Moro Martins, Numerical prediction of the erosion due to particles in elbows, Powder Technology 261 (2014) 105–117.

[16] V. F. Dos Santos, F. J. de Souza, C. A. R. Duarte, Reducing bend erosion with a twisted tape insert, Powder Technology 301 (2016) 889–910.

[17] C. A. R. Duarte, F. J. de Souza, D. N. Venturi, M. Sommerfeld, A numerical assessment of two geometries for reducing elbow erosion, Particuology 49 (2020) 117–133.

[18] C. A. R. Duarte, F. J. de Souza, V. F. dos Santos, Mitigating elbow erosion with a vortex chamber, Powder Technology 288 (2016) 6–25.

[19] C. A. R. Duarte, F. J. de Souza, Innovative pipe wall design to mitigate elbow erosion: A cfd analysis, Wear 380 (2017) 176–190.

[20] S. Turgoose, R. Cottis, K. Lawson, Modeling of electrode processes and surface chemistry in carbon dioxide containing solutions, in: Computer Modeling in Corrosion, ASTM International, 1992.

[21] S. Nešić, Key issues related to modelling of internal corrosion of oil and gas pipelines–a review, Corrosion science 49 (2007) 4308–4338.

[22] R. C. R. da Silva, R. S. Mohamed, A. C. Bannwart, Wettability alteration of internal surfaces of pipelines for use in the transportation of heavy oil via core-flow, Journal of Petroleum Science and Engineering 51 (2006) 17–25.

[23] W. P. Jepson, M. P. Gopal, S. P. Bhongale, Predictive model for sweet corrosion in horizontal multiphase slug flow, CORROSION 96 (1996).

[24] S. Nesic, S. Wang, J. Cai, Y. Xiao, et al., Integrated CO2 corrosion-multiphase flow model, in: SPE International Symposium on Oilfield Corrosion, Society of Petroleum Engineers, 2004.

[25] G. Zhang, Y. Cheng, Electrochemical characterization and computational fluid dynamics simulation of flow-accelerated corrosion of X65 steel in a CO2-saturated oilfield formation water, Corrosion Science 52 (2010) 2716–2724.

[26] H. Hu, Y. F. Cheng, Modeling by computational fluid dynamics simulation of pipeline corrosion in CO2-containing oil-water two phase flow, Journal of Petroleum Science and Engineering 146 (2016) 134–141.

[27] J. Manzanero, C. Redondo, M. Chávez-Módena, G. Rubio, E. Valero, S. Gómez-Álvarez, A. Rivero-Jiménez, High–order discontinuous Galerkin approximation for a three–phase incompressible Navier–Stokes/Cahn–Hilliard model, arXiv preprint arXiv:2012.07722 (2020).

[28] C. W. Hirt, B. D. Nichols, Volume of fluid (VOF) method for the dynamics of free boundaries, Journal of Computational Physics 39 (1981) 201–225.

[29] M. Sussman, P. Smereka, S. Osher, A level set approach for computing solutions to incompressible two-phase flow, Journal of Computational Physics 114 (1994) 146–159.

[30] D. Jacqmin, Calculation of two-phase Navier–Stokes flows using phase-field modeling, Journal of Computational Physics 155 (1999) 96–127.

[31] D. M. Anderson, G. B. McFadden, A. A. Wheeler, Diffuse-interface methods in fluid mechanics, Annual review of fluid mechanics 30 (1998) 139–165.

[32] V. Badalassi, H. Ceniceros, S. Banerjee, Computation of multiphase systems with phase field models, Journal of Computational Physics 190 (2003) 371–397.

[33] J. W. Cahn, J. E. Hilliard, Free energy of a nonuniform system. I. Interfacial free energy, The Journal of chemical physics 28 (1958) 258–267.

[34] F. Boyer, C. Lapuerta, Study of a three component Cahn-Hilliard flow model, ESAIM: Mathematical Modelling and Numerical Analysis-Modélisation Mathématique et Analyse Numérique 40 (2006) 653–687.

[35] D.A. Kopriva, Implementing spectral methods for partial differential equations, Springer Netherlands, 2009.

[36] M. F. Wheeler, An elliptic collocation-finite element method with interior penalties, SIAM Journal on Numerical Analysis 15 (1978) 152–161.

[37] E. Ferrer and R.H.J. Willden, A high order discontinuous Galerkin finite element solver for the incompressible Navier–Stokes equations, Computers & Fluids 46 (2011) 224–230.

[38] E. Ferrer and R. H.J. Willden, A high order discontinuous Galerkin - Fourier incompressible 3D Navier-Stokes solver with rotating sliding meshes, Journal of Computational Physics 231 (2012) 7037–7056.

[39] E. Ferrer, An interior penalty stabilised incompressible Discontinuous Galerkin - Fourier solver for implicit Large Eddy Simulations, Journal of Computational Physics 348 (2017) 754–775.

[40] J. Manzanero, A. M. Rueda-Ramírez, G. Rubio, E. Ferrer, The Bassi Rebay 1 scheme is a special case of the symmetric interior penalty formulation for discontinuous Galerkin discretisations with Gauss–Lobatto points, Journal of Computational Physics 363 (2018) 1–10.

[41] F. Fraysse, C. Redondo, G. Rubio, E. Valero, Upwind methods for the Baer–Nunziato equations and higher-order reconstruction using artificial viscosity, Journal of Computational Physics 326 (2016) 805–827.

[42] C. Redondo, F. Fraysse, G. Rubio, E. Valero, Artificial Viscosity Discontinuous Galerkin Spectral Element Method for the Baer-Nunziato Equations, in: Spectral and High Order Methods for Partial Differential Equations ICOSAHOM 2016, Springer, 2017, pp. 613–625.

[43] S. Gómez-Álvarez, A. Rivero-Jiménez, G. Rubio, J. Manzanero, C. Redondo, et al., Novel Coupled Cahn-Hilliard Navier-Stokes Solver for the Evaluation of Oil and Gas Multiphase Flow, in: BHR 19th International Conference on Multiphase Production Technology, BHR Group, 2019.

[44] J. Manzanero, G. Rubio, D. A. Kopriva, E. Ferrer, E. Valero, Entropy-stable discontinuous Galerkin approximation with summation-by-parts property for the incompressible Navier-Stokes/Cahn-Hilliard system, Journal of Computational Physics (2020) 109363.

[45] J. Manzanero, C. Redondo, G. Rubio, E. Ferrer, E. Valero, S. Gómez-Álvarez, Á. Rivero-Jiménez, A high-order discontinuous Galerkin solver

for multiphase flows, in: Spectral and High Order Methods for Partial Differential Equations ICOSAHOM 2018, Springer, Cham, 2020, pp. 313–323.

[46] J. S. Hesthaven, T. Warburton, Nodal discontinuous Galerkin methods: algorithms, analysis, and applications, Springer Science & Business Media, 2007.

[47] G. Gassner, D. A. Kopriva, A comparison of the dispersion and dissipation errors of Gauss and Gauss–Lobatto discontinuous Galerkin spectral element methods, SIAM Journal on Scientific Computing 33 (2011) 2560–2579.

[48] R. C. Moura, S. J. Sherwin, J. Peiró, Linear dispersion–diffusion analysis and its application to under-resolved turbulence simulations using discontinuous Galerkin spectral/hp methods, Journal of Computational Physics 298 (2015) 695–710.

[49] J. Manzanero, G. Rubio, E. Ferrer, E. Valero, Dispersion-dissipation analysis for advection problems with nonconstant coefficients: Applications to discontinuous Galerkin formulations, SIAM Journal on Scientific Computing 40 (2018) A747–A768.

[50] J. Manzanero, E. Ferrer, G. Rubio, E. Valero, Design of a Smagorinsky spectral vanishing viscosity turbulence model for discontinuous Galerkin methods, Computers & Fluids (2020) 104440.

[51] D. A. Kopriva, Metric identities and the discontinuous spectral element method on curvilinear meshes, Journal of Scientific Computing 26 (2006) 301.

[52] M. Kompenhans, G. Rubio, E. Ferrer, and E. Valero, Comparisons of p–adaptation strategies based on truncation– and discretisation–errors for high order discontinuous Galerkin methods, Computers & Fluids 139 (2016) 36 – 46.

[53] M. Kompenhans, G. Rubio, E. Ferrer, and E. Valero, Adaptation strategies for high order discontinuous Galerkin methods based on tau-estimation, Journal of Computational Physics 306 (2016) 216 – 236.

[54] A. M. Rueda-Ramírez, J. Manzanero, E. Ferrer, G. Rubio, E. Valero, A p-multigrid strategy with anisotropic p-adaptation based on truncation errors for high-order discontinuous Galerkin methods, Journal of Computational Physics 378 (2019) 209–233.

[55] G. J. Gassner, A. R. Winters, D. A. Kopriva, Split form nodal discontinuous Galerkin schemes with summation-by-parts property for the compressible Euler equations, Journal Of Computational Physics 327 (2016) 39–66.

[56] A.R. Winters and G.J. Gassner, Affordable, entropy conserving and entropy stable flux functions for the ideal MHD equations, Journal of Computational Physics 304 (2016) 72 – 108.

[57] J. Manzanero, G. Rubio, E. Ferrer, E. Valero, D. A. Kopriva, Insights on aliasing driven instabilities for advection equations with application to Gauss–Lobatto discontinuous Galerkin methods, Journal of Scientific Computing 75 (2018) 1262–1281.

[58] G. J. Gassner, A. R. Winters, F. J. Hindenlang, D. A. Kopriva, The BR1 scheme is stable for the compressible Navier–Stokes equations, Journal of Scientific Computing 77 (2018) 154–200.

[59] J. Manzanero, G. Rubio, D. A. Kopriva, E. Ferrer, E. Valero, A free-energy stable nodal discontinuous Galerkin approximation with summation-by-parts property for the Cahn-Hilliard equation, Journal of Computational Physics 403 (2020) 109072.

[60] J. Manzanero, G. Rubio, D. A. Kopriva, E. Ferrer, E. Valero, An entropy–stable discontinuous Galerkin approximation for the incompressible Navier–Stokes equations with variable density and artificial compressibility, Journal of Computational Physics 408 (2020) 109241.

[61] B. Bozzini, M. E. Ricotti, M. Boniardi, C. Mele, Evaluation of erosion–corrosion in multiphase flow via cfd and experimental analysis, Wear 255 (2003) 237–245.

[62] J. Manzanero, C. Redondo, G. Rubio, E. Ferrer, A. Jiménez, A discontinuous Galerkin approximation for a wall-bounded consistent three-component Cahn–Hilliard flow model, Under review in Computers and Fluids (2020).

[63] B. Song, C. Plana, J. M. Lopez, M. Avila, Phase-field simulation of core-annular pipe flow, International Journal of Multiphase Flow 117 (2019) 14–24.

[64] P. Sagaut, Large eddy simulation for incompressible flows: an introduction, Springer Science & Business Media, 2006.

[65] R. Röhrig, S. Jakirlić, C. Tropea, Comparative computational study of turbulent flow in a 90 pipe elbow, International Journal of Heat and Fluid Flow 55 (2015) 120–131.

[66] J. Lowengrub, L. Truskinovsky, Quasi–incompressible cahn–hilliard fluids and topological transitions, Proceedings of the Royal Society of London. Series A: Mathematical, Physical and Engineering Sciences 454 (1998) 2617–2654.

[67] J. Shen, Pseudo-compressibility methods for the unsteady incompressible Navier-Stokes equations, in: Proceedings of the 1994 Beijing symposium on nonlinear evolution equations and infinite dynamical systems, 1997, pp. 68–78.

[68] J. Shen, X. Yang, Energy stable schemes for Cahn-Hilliard phase-field model of two-phase incompressible flows, Chinese Annals of Mathematics, Series B 31 (2010) 743–758.

[69] J. Shen, X. Yang, Numerical approximations of Allen-Cahn and Cahn-Hilliard equations, Discrete Contin. Dyn. Syst 28 (2010) 1669–1691.

[70] F. Hindenlang, G. J. Gassner, C. Altmann, A. Beck, M. Staudenmaier, C.-D. Munz, Explicit discontinuous galerkin methods for unsteady problems, Computers & Fluids 61 (2012) 86–93.

[71] G.J. Gassner, A kinetic energy preserving nodal discontinuous Galerkin spectral element method, International Journal for Numerical Methods in Fluids 00 (2013) 1–27.

[72] G. J. Gassner, A. R. Winters, D. A. Kopriva, Split form nodal discontinuous Galerkin schemes with summation-by-parts property for the compressible Euler equations, Journal of Computational Physics 327 (2016) 39–66.

[73] C. A. R. Duarte, F. J. de Souza, V. F. dos Santos, Numerical investigation of mass loading effects on elbow erosion, Powder Technology 283 (2015) 593–606.

[74] C. A. R. Duarte, F. J. de Souza, R. de Vasconcelos Salvo, V. F. dos Santos, The role of inter-particle collisions on elbow erosion, International journal of multiphase flow 89 (2017) 1–22.

[75] P. P. Brown, D. F. Lawler, Sphere drag and settling velocity revisited, Journal of Environmental Engineering 129 (2003) 222–231. doi:10.1061/(ASCE)0733-9372(2003)129:3(222).

[76] M. Sommerfeld, N. Huber, Experimental analysis of modelling of particle-wall collisions, International Journal of Multiphase Flow 25 (1999) 1457–1489. doi:10.1016/S0301-9322(99)00047-6.

[77] S. Kanwar, Study and modeling of sweet corrosion of multiphse mixtures in horizontal pipelines, Ph.D. thesis, Ohio, 1994.

[78] H. Hu, Y. F. Cheng, Modeling by computational fluid dynamics simulation of pipeline corrosion in CO2-containing oil-water two phase flow, Journal of Petroleum Science and Engineering 146 (2016) 134–141.

[79] S. Elghobashi, On predicting particle-laden turbulent flows, Applied Scientific Research 52 (1994) 309–329. doi:10.1007/BF00936835.

[80] C. J. Reagle, Technique for Measuring the Coefficient of Restitution for Microparticle Sand Impacts High Temperature for Turbomachinery Applications, Ph.D. thesis, 2012.

[81] C. B. Solnordal, C. Y. Wong, J. Boulanger, An experimental and numerical analysis of erosion caused by sand pneumatically conveyed through a standard pipe elbow, Wear 336 (2015) 43–57.

[82] O. E. Adedeji, C. A. R. Duarte, Prediction of thickness loss in a standard 90° elbow using erosion-coupled dynamic mesh, Wear 460 (2020) 203400.